THE JOURNAL OF PHYSICAL CHEMISTRY C

Article

pubs.acs.org/JPCC

Reconstruction of the Wet Chemical Synthesis Process: The Case of Fe_5C_2 Nanoparticles

Siyu Yao,[†,¶] Ce Yang,[†,‡,¶] Huabo Zhao,[†] Siwei Li,[†] Lili Lin,[†] Wen Wen,[§] Jinxun Liu,[∥,⊥] Gang Hu,[#] Weixue Li,[∥,⊥] Yanglong Hou,[*,‡] and Ding Ma[*,†]

[†]College of Chemistry and Molecular Engineering and [‡]College of Engineering, Peking University, Beijing 100871, China

[§]Shanghai Institute of Applied Physics, Chinese Academy of Science, Shanghai Synchrotron Radiation Facility (SSRF), Shanghai 201204, China

[∥]Department of Chemical Physics, University of Science and Technology of China, Hefei 230026, China

[⊥]State Key Laboratory of Catalysis, Dalian Institute of Chemical Physics, Chinese Academy of Sciences, Dalian 116023, China

[#]Israel Chemicals Limited, Shanghai 200021, China

Supporting Information

ABSTRACT: Wet chemical synthesis (WCS), especially under high temperatures, is one of the most frequently used strategies for nanostructured material construction, which has been used extensively in medical-, energy-, and environment-related applications. Although knowledge about the WCS process has been accumulated in the past two decades, the high temperature used in the process and multiphase nature of intermediates and products are key factors preventing the processes from rationalization. In this paper, by using multilevel *in situ* cells, we developed a strategy to monitor the reaction details of WCS processed in the solid, liquid, and gas phase simultaneously. This protocol has proven successful to reconstruct the WCS process of Fe_5C_2 nanoparticles (NPs) and unravel the complicated chemistry in the synthesis process.

INTRODUCTION

In a conventional high-temperature wet chemical synthesis (HWCS) process, metal precursors are dispersed in proper solvents (such as oleic acid and amine), with the existence of surfactants. The mixture is then heated for reaction to obtain the targeted nanomaterials.[1−5] The complicated interactions between solvents, precursors, and products make it extremely difficult to rationalize the synthetic chemistry of HWCS process. In previous reports, the formation mechanisms of nanostructured materials synthesized by the HWCS method are mostly derived from indirect electron microscopy and ex-situ XRD observation,[6−9] or from control experiments under different reaction conditions.[10−13] Although these efforts help to understand the synthesis process and sketch out a strategy to prepare new nanomaterials, the off-line methods often provide incomplete or even misleading information. Therefore, the wet chemical synthesis is by far still an art than science. Applying online observation based on time-resolved spectroscopy, scattering and diffraction methods is highly desirable to solve this problem.[14−16] However, the main challenge comes from how to introduce the detection probe without interfering the conventional synthetic process. Microreactors that utilize designs such as capillary tube and droplet have been successfully applied to low-temperature liquid phase synthesis in aqueous solution, as the instrument setup could effectively transpose spatial and temporal information, which benefits kinetic studies.[17−23] However, the microreactors also suffered from laminar flow and poor fluidity. In HWCS using viscous organic medium, the disadvantages are magnified. In addition, it still requires a large effort to design microreactors that could work under inert atmosphere and fit to do the basic operations, such as degassing and hot injection.[24−28]

Hägg iron carbide (Fe_5C_2), particular its nanosized form, is very important in various energy-related processes.[29−38] Conventional strategies of carburization via either solid−solid or solid−gas reactions have difficulties in controlling the size and phase.[39−41] However, HWCS method provides a facile and practical way to address the problems. In our previous work, we reported the controlled synthesis of Fe_5C_2 nanoparticles (NP) by the HWCS process for the first time.[42] In the work, we proposed that the formation of well-crystallized Fe NPs is the key for the synthesis process. But as the understanding was based on the XRD and TEM characterization of limited number of off-line products, the description of the synthetic chemistry is possibly not accurate enough. Using these Fe_5C_2 NPs as an example, we demonstrate here the reconstruction of the HWCS process using *in situ* observation methods. Multiple real-time characterization methods were employed to address

Received: January 7, 2017
Revised: February 11, 2017
Published: February 13, 2017

ACS Publications © 2017 American Chemical Society

DOI: 10.1021/acs.jpcc.7b00198
J. Phys. Chem. C 2017, 121, 5154−5160

the reaction details happening in the solid, liquid, and gas phases (Scheme 1). This sophisticated system allows us to disclose the structural evolution and the accurate synthetic mechanism of Fe_5C_2 NPs for the first time. It can be adopted as a general protocol for the *in situ* investigation of wet chemical synthesis of various nanomaterials

Scheme 1. Schematic Illustration of Home-Made Circulate Apparatus for *Operando* High-Temperature Wet Chemical Synthesis Investigation

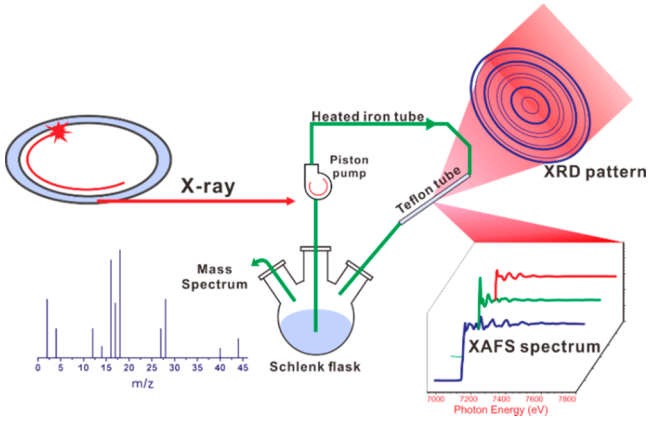

EXPERIMENTAL SECTION

Typical Synthetic Process of Fe_5C_2 NPs. Octadecylamine (30 g) and CTAB (0.226 g) were mixed in a four-neck flask, stirred, and degassed under N_2 flow. The mixture was then heated to 120 °C, followed with the addition of $Fe(CO)_5$ (1 mL, 7.2 mmol) by injection under a N_2 blanket. The mixture was heated to 180 °C at 10 K/min and kept at this temperature for 30 min. A color change from orange to black was observed during the process. Subsequently, the mixture was further heated to 350 °C at 10 K/min and kept at that temperature for 10 min before it was cooled to room temperature. The product was filtered, washed with ethanol and hexane, and collected for further characterization.

***Operando* XRD and Real-Time Mass Spectroscopy.** The time-resolved *operando* XRD data of the synthesis process of Fe_5C_2 NPs were collected at the BL14B1 beamline (λ = 1.2398 Å, 10 keV) of Shanghai Synchrotron Radiation Facility (SSRF). The experiment was done using the homemade *operando* apparatus shown in Scheme 1 (photos of the apparatus were shown in Figure S1). In the *operando* measurement, the synthetic mixture was pumped continuously out of the Schlenk bottle via a piston pump at a flow rate of 20 mL/min, squeezed through a Teflon tube (o.d. = 3 mm, i.d. = 2.0 mm) that served as the XRD cell, and cycled back into the Schlenk bottle. The dead volume of the whole system was determined to be 10 mL. All the iron tubing and the pump were heated using a heating belt to keep the temperature close to that in the reactor. The XRD data collection started 1 min after $Fe(CO)_5$ injection. The time resolution of operando measurement was 90 s/spectrum. Two-dimensional powder XRD patterns were collected with a MAR225 CCD detector and the diffractions were integrated using the Fit2d code.[43] The real-time mass spectroscopy (MS) analysis on the chemical composition of the gas phase products was done using an Omnistarmass spectrometer. The outflow gas from the Schlenk flask was connected to the gas analysis system via capillary tube. The effluent gases were tracked during the whole synthesis process.

***Operando* XANES and XAFS Measurements.** The time-resolved Fe K edge *operando* XANES and XAFS spectra were collected at BL14W beamline of SSRF using QXAFS mode, with the same *operando* setup. The XANES spectrum collection started 1 min after $Fe(CO)_5$ injection. Each shot took 30 s for collection and every 5 shots were merged into one spectrum to improve the quality of spectrum. Fe foil, FeO, and Fe_5C_2 NPs (synthesized and sealed under Ar protection) were employed as standards. All spectra were processed using Athena software inside Ifeffit package.[44] Due to the interference of bubbles generated at around 180 and 280 °C, the quality of QXAFS spectra was insufficient for further structural refinement. To solve this problem, we quenched the reaction using ice bath at those temperatures under parallel conditions to the *operando* measurements and did the XAFS measurements in the air-proof XAFS cell.

***Operando* Transmission Infrared (IR) Spectroscopy.** The time-resolved *operando* transmission IR spectroscopy was done using an instrumental setup similar to the *operando* XRD and XAFS setup on a Bruker Tensor 27 IR spectrometer. Instead of a Teflon tube cell, a home-designed IR liquid cell with CaF_2 windows was utilized for spectrum collection.[45] The thickness of liquid film was tuned with Pb foil to gain appropriate transmittance. The time resolution of *operando* measurement is set as 16 s/spectrum.

GC−MS of the Liquid Phase. The chemical composition of liquid phase at each temperature interval was analyzed using an Agilent 7890A-5975C GC−MS analysis system. Samples were collected and quenched under parallel conditions to the *operando* experiments. Appropriate amount of *n*-eicosane was added in the liquid phase as chemical inert inner-standard to normalize the GC signals.

Transmission Electron Microscopy (TEM). TEM was carried out on an FEI Tecnai T20 microscopy. High-resolution transmission electron microscopy (HRTEM) was carried out on an FEI Tecnai F30 microscopy.

Calculation Methods. All spin-polarized density functional theory (DFT) calculations were performed by using projector augmented wave (PAW)[46] potentials and the Perdew−Burke−Ernzerhof (PBE) functional[47] implemented in the Vienna ab initio simulation package (VASP)[48,49] code. The energy cutoff for the plane wave basis set was 400 eV. The structure optimizations were deemed converged when the forces on each atom were below 0.02 eV/Å. The optimized lattice constant for Fe with body center cubic (BCC) structure is 2.833 Å. Fe (310) surface consisted of B5 site was considered in our calculations. This surface was simulated by using ten atom layers slab models and $p(2\times2)$ unit cell were applied. Neighboring slabs are separated by a vacuum of 15 Å to avoid the interactions between them. We used Monkhorst−Pack mesh *k*-points of 5 × 5 × 1 here. The top five layers of the slabs and the adsorbates were fully relaxed, and dipole correction was adopted.

The improved force reversed method[50] was used to determine the transition states (TS) and the force tolerance of 0.02 eV/Å was used. And some of the TS are verified by climbing-image nudged elastic band (CI-NEB) methods.[51,52] We have adopted the separate adsorption of the species involved as the initial and final states for the elementary reactions in this article.

DOI: 10.1021/acs.jpcc.7b00198
J. Phys. Chem. C 2017, 121, 5154−5160

RESULTS AND DISCUSSION

Infrared spectroscopy (IR) is an ideal tool to study carbonyl and adsorbed CO over the metal catalyst. We first used *in situ* IR to track the structure evolution at the early stage of the synthesis. After injection of $Fe(CO)_5$ into the solvent, typical C═O vibration bands at 2021, 1999, and 1962 cm^{-1} appeared.[53] At 180 °C, with the reaction going on, the intensity of these bands decreased rapidly (Figure 1a), suggesting the fast thermal decomposition of $Fe(CO)_5$. Meanwhile, a new broad band appeared at 1931 cm^{-1}, indicating the increase of π-back-bonding from Fe central atom to CO ligands.[13] This signal is most likely attributed to the coordination between $-NH_2$ (electron donor) of octadecylamine and the Fe carbonyl complexes.[54] New signals at 1946 and 1756 cm^{-1} appeared when the system was kept at 180 °C for around 30 min. These two bands are from the stretch vibration of CO adsorbed at the on-top and 3-fold sites of metallic iron. Although the appearance of CO adsorbed at 3-fold sites suggests the formation of iron clusters, we did not observe any iron species on the *operando* synchrotron XRD profile during this period of time (Figure 1c), which indicates that the size of generated iron species was still under the detection limit of XRD technique (around 2 nm). Significantly, the first two *operando* XANES spectra collected at 180 °C (right after injection of $Fe(CO)_5$ and before temperature ramping) show a relatively low absorption edge energy and low "white-line" intensity (Figure 1e), which suggests that the iron species are near metallic. Meanwhile, the corresponding Fe K-edge EXAFS spectra (Figure 1f and Table S1) show the existence of Fe−Fe coordination (coordination number, N_{Fe-Fe} = 6.9 at 2.75 Å; N_{Fe-Fe} = 0.7 at 2.53 Å) in addition to the Fe−C coordination from the adsorbed CO. This is another evidence for the formation of multinuclear metallic iron clusters upon the decomposition of $Fe(CO)_5$. During this period, online mass spectroscopy (MS) (Figure 2a) has detected the release of CO, whereas the octadecylamine solvent was almost intact at this temperature (see GC−MS in Figure 2d).

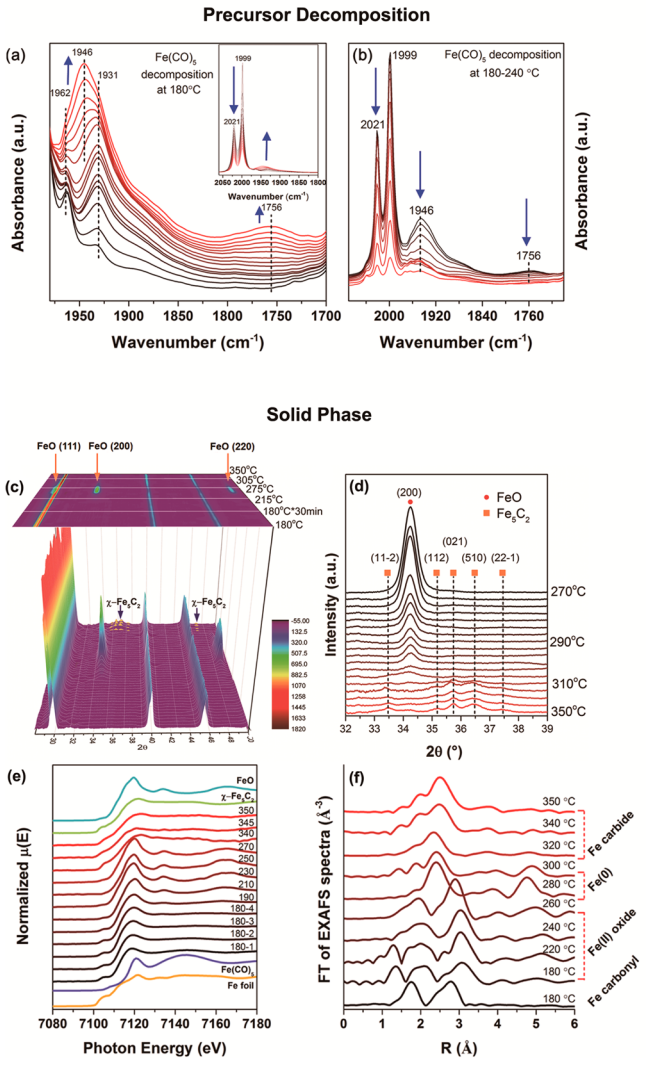

Figure 1. *Operando* characterization of the precursor and solid phase products. In-situ liquid phase FTIR spectra of Fe_5C_2 NPs synthesis (from black to red): spectra in (a) were taken at 180 °C for 30 min; spectra in (b) were collected during the heating stage of 180 to 240 °C. The blue arrows indicate the increase of reaction temperature or the prolonging of reaction time. *Operando* XRD patterns of the HWCS process of χ-Fe_5C_2 NPs (c) and the crystal phase transformation from FeO (270 °C) to Fe_5C_2 (350 °C) (d). The signals at 29.9°, 39.8°, and 45.4° are background from crystal polytetrafluoroethylene in the Teflon tube. The reflections of χ-Fe_5C_2 in (c) were highlight in yellow. *Operando* Fe K edge XANES of χ-Fe_5C_2 synthesis (e) and Fourier-transformation EXAFS spectra of parallel measurement (f).

After 240 °C, all the IR bands disappeared, indicating the full conversion of precursors (Figure 1b). In the liquid phase (Figure 2d), nothing but the original solvent was detected before the temperature reached 215 °C. At this temperature, the reflections of cubic FeO ($Fm\bar{3}m$ space group, JCPDS No. 89−0690) at 28.8°, 33.4°, and 47.9° suddenly appeared (Figure 1c), indicating the formation of FeO NPs over 5 nm (see also the TEM images in Figure S2). The intensity of the FeO NPs increased with temperature elevation and reached a maximum at about 270 °C, which was associated with the size growth of FeO crystal (to about 20 nm). We attribute the formation of FeO intermediates to the oxidative nucleation/growth process under limited O chemical potential (the solution was degassed before reaction). It is worthwhile to note that Fe oxide particles would became final products if the oxygen removal is not executed.

The Fe K-edge EXAFS results highly support the oxidative nucleation hypothesis (Figure 1e,f and Table S1). At the very early stage of the reaction, i.e., 30 min reaction at 180 °C (Table S1, entry 2), the bonding of oxygen on Fe could already be observed (N_{Fe-O} = 3.8). Meanwhile, the existence of partially oxidized Fe(II) was resolved at 190 °C as the typical feature of FeO (7134 eV) appeared in XANES (Figure 1e),[55] indicating that the oxidation of iron occurred gradually with the thermal decomposition of iron carbonyl precursor and formation of iron clusters (Figure 1e). By comparison with standard FeO pattern and Fe foil, the linear combination fit (LCF) result of the XANES spectrum suggests the system is composed by 63% of Fe(II) and 37% of metallic iron at 190 °C. With the reaction temperature further increased, this trend becomes more obvious with the composition of Fe(II) increased and reached 100% from 230 to 270 °C. EXAFS as well as XRD and TEM results suggest that the size of FeO particles is around 20 nm at 220 °C with N_{Fe-O} = 5.8 and N_{Fe-Fe} around 9, and becomes even larger with the temperature increased to 260 °C (Table S1, entry 3).

With a further increase of reaction temperature above 270 °C, however, the XRD signals of FeO dropped dramatically and finally disappeared at around 300 °C. Meanwhile, the

DOI: 10.1021/acs.jpcc.7b00198
J. Phys. Chem. C 2017, 121, 5154−5160

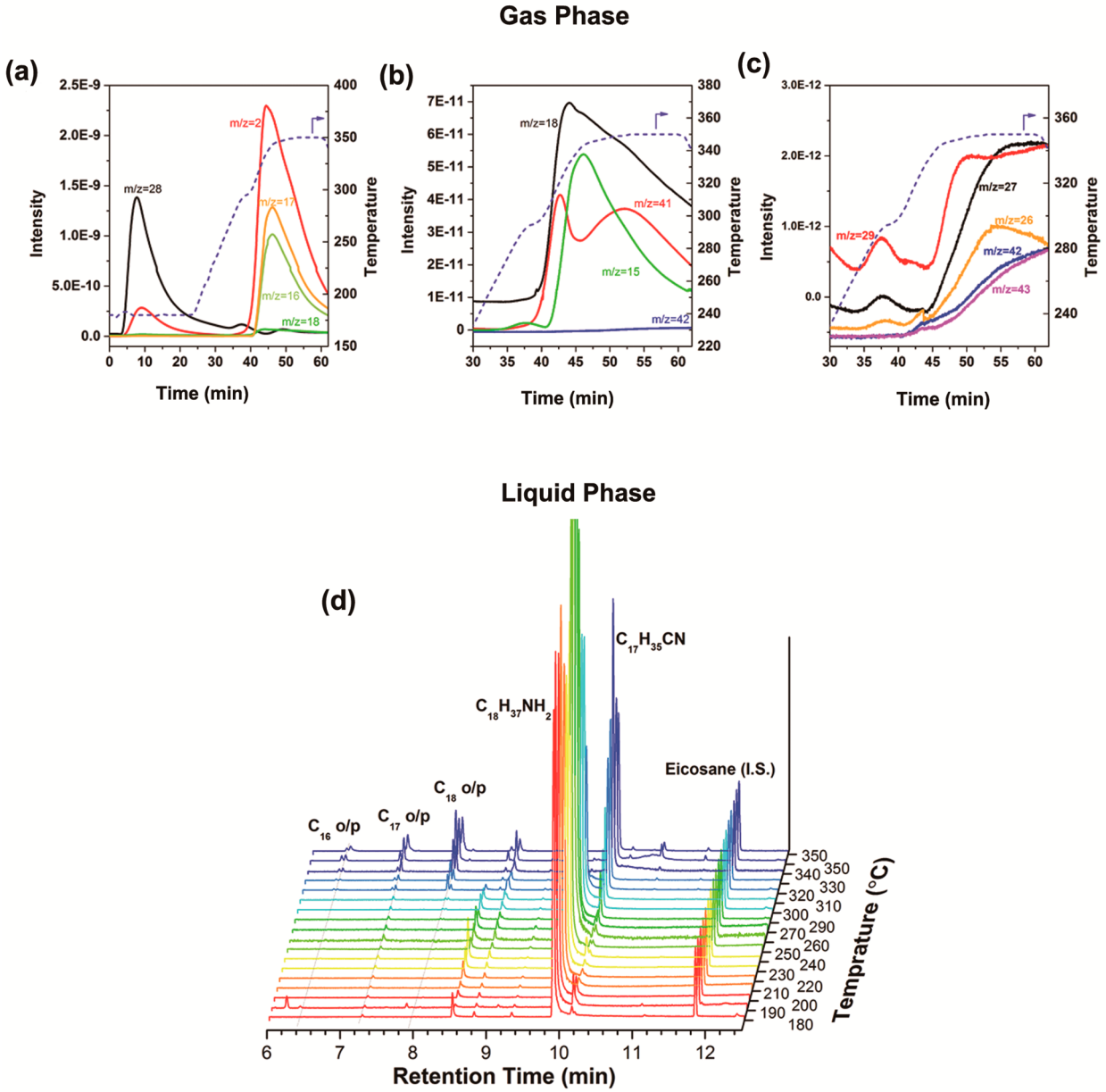

Figure 2. Online MS and GC−MS of the gas phase. Major products (a), main intermediates (b), and generation of light hydrocarbon compounds (c). GC−MS profiles of liquid phase at different reaction temperatures (d).

reflections of χ-Fe_5C_2 in the range 36−38° gradually appeared at 310−320 °C and grew stronger in intensity until 350 °C (JCPDS No. 36-1248), which is also confirmed by corresponding XANES spectra (Figure 2a).[56,57]

Although the XRD results indicate the conversion process at this stage is simple, it is still hard to understand the chemistry behind this phase evolution as iron carbide is normally regarded as a metallic crystal with interstitial carbon atoms. To understand this process, one needs to find out (1) how the oxygen was deprived of from FeO crystals, (2) what is the source of carbon in iron carbide, and (3) what the sequence of the process is. Analysis of the products from the gas phase as well as the liquid phase provides important clues for these issues.

The GC−MS chromatogram of the liquid phase proved that the initial state at 180 °C is mainly the solvent $C_{18}H_{37}NH_2$ (retention time = 9.9 min, Figure 2d). The cation of $C_{16}H_{33}N(CH_3)_3$ appeared at 8.5 min, which was associated with the addition of CTAB. The chemical composition of the liquid phase remained stable until 270 °C, when $C_{17}H_{35}CN$ (retention time = 10.2 min), the dehydrogenation product of $C_{18}H_{37}NH_2$, appeared. The peak of $C_{18}H_{37}NH_2$ disappeared at 330 °C, indicating the complete conversion of $C_{18}H_{37}NH_2$ into $C_{17}H_{35}CN$. Meanwhile, a series of peaks of C_{16}−C_{18} olefin and paraffin products appeared at 320 °C with the intensity increased with higher temperatures. Those alkane and alkene products were generated via the C−N and C−C cleavage of $C_{18}H_{37}NH_2$ or $C_{17}H_{35}CN$ at relatively high temperatures (evidence of corresponding fragments have been track by online MS). As pure $C_{18}H_{37}NH_2$ has good thermal stability,[6] it can be concluded that the dehydrogenation and C−C cleavage reactions are actually catalyzed by the iron species in the system. When correlating the GC−MS results with the structural evolution, we found that the $C_{18}H_{37}NH_2$ dehydro-

DOI: 10.1021/acs.jpcc.7b00198
J. Phys. Chem. C 2017, 121, 5154−5160

genation occurred at a similar temperature of FeO disappearance indicated by XRD, suggesting that FeO was possibly reduced by the molecular hydrogen generated from the dehydrogenation reaction (the possibility of direct hydrogen transfer from solvent to FeO cannot be excluded).

In the gas phase, the MS signal of H_2 (m/z = 2) started increasing dramatically from 260 °C (Figure 3a). The intensity of the product with m/z = 41 increased with temperature while the intensity of m/z = 42 signal did not exhibit a similar trend (Figure 2bc). It is therefore clear that the m/z = 41 species is not related with propene but acetonitrile (CH_3CN) which generated via the dehydrogenation and α, β C−C bond cleavage of $C_{18}H_{37}NH_2$. This could be demonstrated by a similar trend of HCN signal (m/z = 26) with that of acetonitrile. These phenomena, together with the GC−MS results ($C_{17}H_{35}CN$ generation), confirmed that $C_{18}H_{37}NH_2$ actually underwent dehydrogenation and served as the hydrogen source to remove the oxygen in FeO NPs (either intermolecular hydrogen transfer or reduction by gas phase H_2). The good correlation of the water (m/z = 18) generation temperature with spectroscopy evidence of FeO reduction serves as powerful evidence.

By far, there is one remaining question to be answered; i.e., did carbon atoms enter the lattice of FeO at the same time of oxygen removal? At 280 °C, when a large amount H_2 was generated (Figure 2a), the EXAFS spectra showed that the FeO phase was reduced to the metallic iron (Fe−Fe at 2.44 and 2.79 Å) state (Figure 1f and Table S1 entries 6,7). The freshly reduced Fe(0) was in the form of small particles as the average Fe−Fe coordination number is around 4.5. These particles were below the detection limit of XRD. However, the drastic formation of the large amount of Fe(0) particles led to an intensive structural disintegration of iron oxide and the quick disappearance of crystal FeO diffraction peaks (Figure 1c). After that, the formation of Fe−C bonding was observed at 320 °C, indicating amorphous Fe(0) clusters are the precursor for pure phase χ-Fe_5C_2. In the gas phase, we observed the formation of a serial of C_{2-3} alkane and alkene from 320 °C until the end of reaction, which was the pyrolysis fragments of $C_{17}H_{35}CN$ and other intermediates. On the contrary, methane was generated below 300 °C, which means the carburization of Fe_5C_2 NPs was probably related with C_{2-3} fragments instead of methane. For verification, we calculated the adsorption energy and C−H bond dissociation barrier of methane and C_{2-3} (with ethene as an example) on the stepped Fe (310) surface at 320 °C by the density functional theory (DFT) method (Figure S3−5). The calculation results clearly show that the adsorption of ethene (model molecule for C_{2-3} fragments) is thermodynamically and kinetically more favorable than that of methane. The dissociation of ethene into atomic carbon also has a much lower barrier than methane. As a result, Fe(0) is probably carburized by C_{2-3} fragments. To further confirm this conclusion, a control experiment was designed by holding the temperature of the synthetic system at 300 °C (temperature for the formation of metallic iron NPs) and bubbling diluted ethylene into the solution for 30 min. The XRD profile suggested that the product was Fe_5C_2 (Figure S6), whereas the reaction stopped with the formation of metallic iron NPs when methane was introduced instead. This result confirms the speculation that C_{2-3} fragments are the carbon source for the carburization process. In other word, the carburization temperature is mainly controlled by the pyrolysis temperature of the solvents.

The combined *in situ* characterization sketched a vivid picture of the complicated oxidation state change and structural evolution of iron species during the HWCS process. The overall evolution of NPs and solvent during the reaction is illustrated in Scheme 2. It demonstrates that the interplay

Scheme 2. Schematic Illustration of Evolution of NPs and Solvent during the Reaction

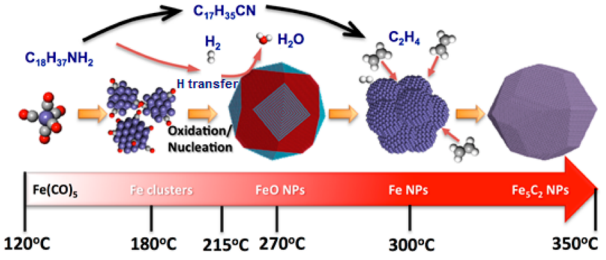

between iron species and the organic solvent plays a vital role, as the generated nanostructures catalyze the transformation of organic solvent *in situ*. It is worth noting that it is equally or even more important to understand the role of organic solvent in the synthetic process because the organic media provides the hydrogenation agent as well as carbon source for Fe_5C_2, which serves as the driven force for the phase transformation of the materials. Third, the synthetic temperature, as a necessary factor that triggers the mentioned reactions, directly determines the crystal phase of products. Changing the ramping rate may prolong or shorten certain chemical transformation stages and further influence the structure of final particles. On the basis of our understandings gained from the Fe_5C_2 system, we have managed to extend the synthetic protocol to other transition metal carbide nanostructures such as MoC and Co_2C NPs (Figure S7).

CONCLUSION

In summary, we utilized a multilevel online cell to monitor the synthetic details happened in solid, liquid, and gas phases using multiple *operando* characterization methods. Utilizing this setup, we managed to reconstruct the formation mechanism of Fe_5C_2 NPs by the combination of *operando* IR, XRD, XAS, and MS methods for the first time. The *operando* observation discloses that FeO is an important intermediate phase in Fe_5C_2 NPs synthesis, which was not observed by previous off-line attempt. It is expected that this strategy can be used as a general protocol for mechanism study of the wet chemical synthesis processes.

ASSOCIATED CONTENT

Supporting Information

The Supporting Information is available free of charge on the ACS Publications website at DOI: 10.1021/acs.jpcc.7b00198.

Photos of homemade *in situ* flow system, TEM and HRTEM of iron, cobalt, and molybdenum carbide materials, transition state geometries, potential energy diagrams, XRD patterns, EXAFS fitting results of Fe K edge spectra (PDF)

AUTHOR INFORMATION

Corresponding Authors

*D. Ma. E-mail: dma@pku.edu.cn.

*Y. Hou. E-mail: hou@pku.edu.cn.

DOI: 10.1021/acs.jpcc.7b00198
J. Phys. Chem. C 2017, 121, 5154−5160

ORCID

Weixue Li: 0000-0002-5043-3088

Ding Ma: 0000-0002-3341-2998

Author Contributions

[¶]The manuscript was written through contributions of all authors. All authors have given approval to the final version of the manuscript. S.Y and C.Y contributed equally.

Notes

The authors declare no competing financial interest.

■ ACKNOWLEDGMENTS

This work was funded by the Natural Science Foundation of China (91645115, 21473003, 21222306, 51590882, 51172005, and 21321002) and 973 Project (2013CB933100, 2013CB834603). The XRD and XAFS experiments were conducted in SSRF and BSRF. C. Yang acknowledges the financial support of China Postdoctoral Science Foundation (Grant No. 2015M580011).

■ REFERENCES

(1) Zhang, J. T.; Tang, Y.; Lee, K.; Min, O. Y. Nonepitaxial Growth of Hybrid Core-Shell Nanostructures with Large Lattice Mismatches. *Science* **2010**, *327*, 1634−1638.

(2) Zherebetskyy, D.; Scheele, M.; Zhang, Y. J.; Bronstein, N.; Thompson, C.; Britt, D.; Salmeron, M.; Alivisatos, P.; Wang, L. W. Hydroxylation of the Surface of PbS Nanocrystals Passivated with Oeic Acid. *Science* **2014**, *344*, 1380−1384.

(3) Zheng, H. M.; Rivest, J. B.; Miller, T. A.; Sadtler, B.; Lindenberg, A.; Toney, M. F.; Wang, L. W.; Kisielowski, C.; Alivisatos, A. P. Observation of Transient Structural-Transformation Dynamics in a Cu_2S Nanorod. *Science* **2011**, *333*, 206−209.

(4) Chen, G. X.; Zhao, Y.; Fu, G.; Duchesne, P. N.; Gu, L.; Zheng, Y. P.; Weng, X. F.; Chen, M. S.; Zhang, P.; Pao, C. W.; et al. Interfacial Effects in Iron-Nickel Hydroxide-Platinum Nanoparticles Enhance Catalytic Oxidation. *Science* **2014**, *344*, 495−499.

(5) Wu, L. H.; Li, Q.; Wu, C. H.; Zhu, H. Y.; Mendoza-Garcia, A.; Shen, B.; Guo, J. H.; Sun, S. H. Stable Cobalt Nanoparticles and Their Monolayer Array as an Efficient Electrocatalyst for Oxygen Evolution Reaction. *J. Am. Chem. Soc.* **2015**, *137*, 7071−7074.

(6) Yin, Y.; Alivisatos, A. P. Colloidal Nanocrystal Synthesis and the Organic-inorganic Interface. *Nature* **2005**, *437*, 664−670.

(7) Chaudhuri, R. G.; Paria, S. Core/Shell Nanoparticles: Classes, Properties, Synthesis Mechanisms, Characterization, and Applications. *Chem. Rev.* **2012**, *112*, 2373−2433.

(8) Mourdikoudis, S.; Liz-Marzan, L. M. Oleylamine in Nanoparticle Synthesis. *Chem. Mater.* **2013**, *25*, 1465−1476.

(9) Zheng, N.; Fan, J.; Stucky, G. D. One-step One-phase Synthesis of Monodisperse Noble-metallic Nanoparticles and their Colloidal Crystals. *J. Am. Chem. Soc.* **2006**, *128*, 6550−6551.

(10) Liu, Y. D.; Tang, A. W.; Zhang, Q.; Yin, Y. D. Seed-Mediated Growth of Anatase TiO_2 Nanocrystals with Core-Antenna Structures for Enhanced Photocatalytic Activity. *J. Am. Chem. Soc.* **2015**, *137*, 11327−11339.

(11) Yin, Y. D.; Rioux, R. M.; Erdonmez, C. K.; Hughes, S.; Somorjai, G. A.; Alivisatos, A. P. Formation of Hollow Nanocrystals through the Nanoscale Kirkendall Effect. *Science* **2004**, *304*, 711−714.

(12) Sun, S. H.; Zeng, H. Size-controlled Synthesis of Magnetite Nanoparticies. *J. Am. Chem. Soc.* **2002**, *124*, 8204−8205.

(13) Kovalenko, M. V.; Bodnarchuk, M. I.; Lechner, R. T.; Hesser, G.; Schaffler, F.; Heiss, W. Fatty Acid Salts as Stabilizers in Size- and Shape-controlled Nanocrystal Synthesis: The Case of Inverse Spinel Iron Oxide. *J. Am. Chem. Soc.* **2007**, *129*, 6352−6353.

(14) Sai Krishna, K.; Navin, C. V.; Biswas, S.; Singh, V.; Ham, K.; Bovenkamp, G. L.; Theegala, C. S.; Miller, J. T.; Spivey, J. J.; Kumar, C. S. Millifluidics for Time-resolved Mapping of The Growth of Gold Nanostructures. *J. Am. Chem. Soc.* **2013**, *135*, 5450−5456.

(15) Thanh, N. T.; Maclean, N.; Mahiddine, S. Mechanisms of Nucleation and Growth of Nanoparticles in Solution. *Chem. Rev.* **2014**, *114*, 7610−7630.

(16) Saha, D.; Jensen, K. M. O.; Tyrsted, C.; Bojesen, E. D.; Mamakhel, A. H.; Dippel, A. C.; Christensen, M.; Iversen, B. B. In Situ Total X-Ray Scattering Study of WO_3 Nanoparticle Formation under Hydrothermal Conditions. *Angew. Chem., Int. Ed.* **2014**, *53*, 3667−3670.

(17) Engelke, L.; Schaefer, M.; Porsch, F.; Bensch, W. In-situ Energy-dispersive X-ray Diffraction Studies of Crystal Growth and Compound Conversion under Solvothermal Conditions. *Eur. J. Inorg. Chem.* **2003**, *2003*, 506−513.

(18) Jensen, H.; Bremholm, M.; Nielsen, R. P.; Joensen, K. D.; Pedersen, J. S.; Birkedal, H.; Chen, Y. S.; Almer, J.; Sogaard, E. G.; Iversen, S. B.; et al. In situ High-energy Synchrotron Radiation Study of Sol-gel Nanoparticle Formation in Supercritical Fluids. *Angew. Chem., Int. Ed.* **2007**, *46*, 1113−1116.

(19) Staniuk, M.; Hirsch, O.; Kranzlin, N.; Bohlen, R.; van Beek, W.; Abdala, P. M.; Koziej, D. Puzzling Mechanism behind a Simple Synthesis of Cobalt and Cobalt Oxide Nanoparticles: In Situ Synchrotron X-ray Absorption and Diffraction Studies. *Chem. Mater.* **2014**, *26*, 2086−2094.

(20) Engelke, L.; Schaefer, M.; Schur, M.; Bensch, W. In situ X-ray Diffraction Studies of the Crystallization of Layered Manganese Thioantimonates(III) under Hydrothermal Conditions. *Chem. Mater.* **2001**, *13*, 1383−1390.

(21) Zhou, Y.; Lin, Y. H.; Patzke, G. R. Synchrotron Radiation for the Study of Hydrothermal Formation Mechanisms of Oxide Nanomaterials. *Prog. Chem.* **2012**, *24*, 1583−1591.

(22) Polte, J.; Erler, R.; Thunemann, A. F.; Sokolov, S.; Ahner, T. T.; Rademann, K.; Emmerling, F.; Kraehnert, R. Nucleation and Growth of Gold Nanoparticles Studied via in situ Small Angle X-ray Scattering at Millisecond Time Resolution. *ACS Nano* **2010**, *4*, 1076−1082.

(23) Polte, J.; Ahner, T. T.; Delissen, F.; Sokolov, S.; Emmerling, F.; Thunemann, A. F.; Kraehnert, R. Mechanism of Gold Nanoparticle Formation in the Classical Citrate Synthesis Method Derived from Coupled In Situ XANES and SAXS Evaluation. *J. Am. Chem. Soc.* **2010**, *132*, 1296−1301.

(24) Liu, F.; Zhu, J. H.; Yang, W. L.; Dong, Y. H.; Hou, Y. L.; Zhang, C. Z.; Yin, H.; Sun, S. H. Building Nanocomposite Magnets by Coating a Hard Magnetic Core with a Soft Magnetic Shell. *Angew. Chem., Int. Ed.* **2014**, *53*, 2176−2180.

(25) Liu, F.; Dong, Y. H.; Yang, W. L.; Yu, J.; Xu, Z. C.; Hou, Y. L. Exchange-Coupled fct-FePd/alpha-Fe Nanocomposite Magnets Converted from Pd/Fe_3O_4 Core/Shell Nanoparticles. *Chem. - Eur. J.* **2014**, *20*, 15197−15202.

(26) Peng, S.; Wang, C.; Xie, J.; Sun, S. Synthesis and Stabilization of Monodisperse Fe Nanoparticles. *J. Am. Chem. Soc.* **2006**, *128*, 10676−10677.

(27) Wang, C. M.; Baer, D. R.; Amonette, J. E.; Engelhard, M. H.; Antony, J.; Qiang, Y. Morphology and Electronic Structure of the Oxide Shell on the Surface of Iron Nanoparticles. *J. Am. Chem. Soc.* **2009**, *131*, 8824−8832.

(28) Liu, Y.; Wang, C.; Wei, Y. J.; Zhu, L. Y.; Li, D. G.; Jiang, J. S.; Markovic, N. M.; Stamenkovic, V. R.; Sun, S. H. Surfactant-Induced Postsynthetic Modulation of Pd Nanoparticle Crystallinity. *Nano Lett.* **2011**, *11*, 1614−1617.

(29) Torres Galvis, H. M.; Bitter, J. H.; Davidian, T.; Ruitenbeek, M.; Dugulan, A. I.; de Jong, K. P. Iron Particle Size Effects for Direct Production of Lower Olefins from Synthesis Gas. *J. Am. Chem. Soc.* **2012**, *134*, 16207−16215.

(30) de Smit, E.; Cinquini, F.; Beale, A. M.; Safonova, O. V.; van Beek, W.; Sautet, P.; Weckhuysen, B. M. Stability and Reactivity of chi-theta- Iron Carbide Catalyst Phases in Fischer−Tropsch Synthesis: Controlling μ(c). *J. Am. Chem. Soc.* **2010**, *132*, 14928−41.

(31) Hu, Y.; Jensen, J. O.; Zhang, W.; Cleemann, L. N.; Xing, W.; Bjerrum, N. J.; Li, Q. Hollow Spheres of Iron Carbide Nanoparticles Encased in Graphitic Layers as Oxygen Reduction Catalysts. *Angew. Chem., Int. Ed.* **2014**, *53*, 3675−9.

DOI: 10.1021/acs.jpcc.7b00198
J. Phys. Chem. C 2017, 121, 5154−5160

(32) Xiao, M.; Zhu, J.; Feng, L.; Liu, C.; Xing, W. Meso/macroporous Nitrogen-doped Carbon Architectures with Iron Carbide Encapsulated in Graphitic Layers as an Efficient and Robust Catalyst for the Oxygen Reduction Reaction in both Acidic and Alkaline solutions. *Adv. Mater.* **2015**, *27*, 2521−2527.
(33) Santos, V. P.; Wezendonk, T. A.; Jaen, J. J.; Dugulan, A. I.; Nasalevich, M. A.; Islam, H. U.; Chojecki, A.; Sartipi, S.; Sun, X.; Hakeem, A. A.; et al. Metal organic framework-mediated synthesis of highly active and stable Fischer−Tropsch catalysts. *Nat. Commun.* **2015**, *6*, 6451.
(34) Xu, K.; Sun, B.; Lin, J.; Wen, W.; Pei, Y.; Yan, S.; Qiao, M.; Zhang, X.; Zong, B. epsilon-Iron Carbide as a Low-temperature Fischer−Tropsch Synthesis Catalyst. *Nat. Commun.* **2014**, *5*, 5783.
(35) Huang, G. M.; Hu, J.; Zhang, H.; Zhou, Z. J.; Chi, X. Q.; Gao, J. H. Highly Magnetic Iron Carbide Nnoparticles as Effective T-2 Contrast Agents. *Nanoscale* **2014**, *6*, 726−730.
(36) Meffre, A.; Mehdaoui, B.; Kelsen, V.; Fazzini, P. F.; Carrey, J.; Lachaize, S.; Respaud, M.; Chaudret, B. A Simple Chemical Route toward Monodisperse Iron Carbide Nanoparticles Displaying Tunable Magnetic and Unprecedented Hyperthermia Properties. *Nano Lett.* **2012**, *12*, 4722−4728.
(37) Hong, S. Y.; Chun, D. H.; Yang, J.; Jung, H.; Lee, H.; Hong, S.; Jang, S.; Lim, J. T.; Kim, C.; Park, J. C. A New Synthesis of Carbon Encapsulated Fe_5C_2 Nanoparticles for High-temperature Fischer−Tropsch Synthesis. *Nanoscale* **2015**, *7*, 16616−16620.
(38) Yu, G. B.; Sun, B.; Pei, Y.; Xie, S. H.; Yan, S. R.; Qiao, M. H.; Fan, K. N.; Zhang, X. X.; Zong, B. N. Fe_xO_y@C Spheres as an Excellent Catalyst for Fischer−Tropsch Synthesis. *J. Am. Chem. Soc.* **2010**, *132*, 935−937.
(39) Browning, L. C.; Dewitt, T. W.; Emmett, P. H. Equilibria in the Systems Fe_2C—Fe—CH_4—H_2 and Fe_3C—Fe—CH_4—H_2. *J. Am. Chem. Soc.* **1950**, *72*, 4211.
(40) Browning, L. C.; Emmett, P. H. Equilibrium Measurements in the System C-CH_4-H_2. *J. Am. Chem. Soc.* **1951**, *73*, 581.
(41) Stencel, J. M.; Eklund, P. C.; Bi, X. X.; Davis, B. H.; Hager, G. T.; Derbyshire, F. J. Carbide Catalysts: Laser Pyrolysis Synthesis and Catalytic Activity. *Stud. Surf. Sci. Catal.* **1993**, *75*, 1797−1800.
(42) Yang, C.; Zhao, H. B.; Hou, Y. L.; Ma, D. Fe_5C_2 Nanoparticles: A Facile Bromide-Induced Synthesis and as an Active Phase for Fischer−Tropsch Synthesis. *J. Am. Chem. Soc.* **2012**, *134*, 15814−15821.
(43) Hammersley, A. FIT2D: an Introduction and Overview. European Synchrotron Radiation Facility Internal Report ESRF97-HA02T 1997.
(44) Ravel, á.; Newville, M. ATHENA, ARTEMIS, HEPHAESTUS: Data Analysis for X-ray Absorption Spectroscopy using IFEFFIT. *J. Synchrotron Radiat.* **2005**, *12*, 537−541.
(45) Wang, H.; Cai, Z.; Zhong, M.; Yao, S.; Kou, Y. In situ FTIR Study of Low-pressure Hydroformylation of 1-hexene Catalyzed by Ultrafine Cobalt Nanoparticles. *Chin. J. Cata.* **2013**, *34*, 781−788.
(46) Blochl, P. E. Projector Augmented-wave Method. *Phys. Rev. B: Condens. Matter Mater. Phys.* **1994**, *50*, 17953−17979.
(47) Perdew, J. P.; Burke, K.; Ernzerhof, M. Generalized Gradient Approximation Made Simple. *Phys. Rev. Lett.* **1996**, *77*, 3865−3868.
(48) Kresse, G.; Hafner, J. Ab initio Molecular Dynamics for Open-shell Transition Metals. *Phys. Rev. B: Condens. Matter Mater. Phys.* **1993**, *47*, 558−561.
(49) Kresse, G.; Furthmüller, J. Efficient Iterative Schemes for *ab initio* Total-energy Calculations using a Plane-wave Basis Set. *Phys. Rev. B: Condens. Matter Mater. Phys.* **1996**, *54*, 11169−11186.
(50) Sun, K.; Zhao, Y.; Su, H. Y.; Li, W. X. Force Reversed Method for Locating Transition States. *Theor. Chem. Acc.* **2012**, *131*, 1118−1127.
(51) Henkelman, G.; Uberuaga, B. P.; Jónsson, H. A Climbing Image Nudged Elastic Band Method for Finding Saddle Points and Minimum Energy Paths. *J. Chem. Phys.* **2000**, *113*, 9901−9904.
(52) Henkelman, G.; Jónsson, H. Improved Tangent Estimate in the Nudged Elastic Band Method for Finding Minimum Energy Paths and Saddle Points. *J. Chem. Phys.* **2000**, *113*, 9978−9985.
(53) Sheline, R. K.; Pitzer, K. S. The Infrared Spectra and Structures of the Iron Carbonyls 1. *J. Am. Chem. Soc.* **1950**, *72*, 1107−1112.
(54) Moore, D. T.; Oomens, J.; Eyler, J. R.; Meijer, G.; von Helden, G.; Ridge, D. P. Gas-phase IR Spectroscopy of Anionic Iron Carbonyl Clusters. *J. Am. Chem. Soc.* **2004**, *126*, 14726−14727.
(55) Paris, E.; Tyson, T. A. Iron Site Geometry in Orthopyroxene: Multiple Scattering Calculations and XANES Study. *Phys. Chem. Miner.* **1994**, *21*, 299−308.
(56) Ribeiro, M. C.; Jacobs, G.; Davis, B. H.; Cronauer, D. C.; Kropf, A. J.; Marshall, C. L. Fischer−Tropsch Synthesis: An In-Situ TPR-EXAFS/XANES Investigation of the Influence of Group I Alkali Promoters on the Local Atomic and Electronic Structure of Carburized Iron/Silica Catalysts. *J. Phys. Chem. C* **2010**, *114*, 7895−7903.
(57) Ribeiro, M. C.; Jacobs, G.; Pendyala, R.; Davis, B. H.; Cronauer, D. C.; Kropf, A. J.; Marshall, C. L. Fischer−Tropsch Synthesis: Influence of Mn on the Carburization Rates and Activities of Fe-Based Catalysts by TPR-EXAFS/XANES and Catalyst Testing. *J. Phys. Chem. C* **2011**, *115*, 4783−4792.

DOI: 10.1021/acs.jpcc.7b00198
J. Phys. Chem. C 2017, 121, 5154−5160